2020

Viscoelastic Analysis of High Strain Composites for Deployable Structures in Space Applications

Andrew Gomez-Delrio
University of Central Florida

VISCOELASTIC ANALYSIS OF HIGH STRAIN COMPOSITES FOR DEPLOYABLE STRUCTURES IN SPACE APPLICATIONS

by

ANDREW GOMEZ-DELRIO
B.S.A.E. University of Central Florida

A thesis submitted in partial fulfilment of the requirements
for the degree of Master of Science in Aerospace Engineering
in the Department of Mechanical and Aerospace Engineering
in the College of Engineering and Computer Science
at the University of Central Florida
Orlando, Florida

Summer Term
2020

Major Professor: Kawai Kwok

ABSTRACT

Thin-ply composite laminates capable of enduring high strains are currently under investigation for compliant deployable spacecraft structures. Deployable structures such as booms fabricated from these materials can be flattened and coiled to high curvatures, achieving a compact configuration for stowage. Once in orbit, they are released with minimal actuation for deployment, allowing the operational geometry to be recovered. Previous studies have shown that the viscoelastic properties of the composite epoxy matrix can negatively impact final shape accuracy due to stress relaxation during stowage. In addition, since the strain energy stored is relied upon for deployment, considerable relaxation can potentially result in deployment stall. Stress relaxation in composites and the aforementioned effects it can have on deployment have not been analyzed sufficiently for space applications. The objective of this thesis is to investigate the moment relaxation and curvature recovery behavior of thin-ply composite laminates through a combination of analytical, numerical, and experimental approaches. The viscoelastic Kirchhoff plate model that serves as the theoretical basis of the analyses is first presented. An analytical solution for the recovery of a composite plate after stowage is derived. The numerical integration of the viscoelastic plate constitutive equations and its implementation as a user-defined subroutine in finite element programs is then described. The subroutine allows relaxation of 3D thin-shell structures to be modeled, and is applied to simulate stowage and recovery of a thin-ply composite currently of interest for solar sailing applications. The subroutine is then compared with results obtained from experiments for a thin-ply composite for bending relaxation and curvature creep recovery after being unloaded.

ACKNOWLEDGMENTS

First and foremost, I would like to thank my advisor Kawai Kwok for providing his mentorship and support over the last few years. His dedication to helping students grow as researchers has given me the ability to thrive as a graduate student and provided countless opportunities I would not have had otherwise. His previous work has set the foundation for what continues to be an interesting and challenging problem that I have had the pleasure of working towards better understanding.

I would also like to gratefully recognize Juan M. Fernandez of NASA Langley Research Center for his guidance during the course of this research. Through many helpful discussions, his willingness to lend his time and assistance has proved vital to my understanding and grasp of the problem investigated herewidth. Moreover, his supplying of the fixtures and materials for testing made acquiring all experimental results possible.

Funding under NASA's Space Grant Consortium's Master's Fellowship for the academic year of 2018-19 is also gratefully acknowledged, as well as funding from Langley Research Center that was provided in support of this work.

TABLE OF CONTENTS

LIST OF FIGURES

LIST OF TABLES

CHAPTER 1: INTRODUCTION

Deployable space structures are designed to be packaged and stowed for launch and subsequently deployed into their operational geometry once in orbit. Although power, communication, and propulsion demands typically require large structures to support mission capabilities, launch vehicle mass and volume constraints must not be exceeded. To enforce the opposing dimensional requirements of payload standards and mission performance, components such as solar arrays and antennas can be integrated with a deployable supporting structure. Lattice deployable structures are commonly employed, which are comprised of rigid links connected by articulated joints and hinges, allowing the structure's configuration to be mechanically controlled [1]. However, as spacecraft systems have become smaller, dramatic reductions in satellite size and cost have occurred. Consequently, a demand for advanced deployable concepts has been realized to achieve packaging ratios that traditional lattice structures with rigid links cannot achieve.

Strain energy deployable boom concepts have been developed for spacecraft applications since the 1960's [2] to achieve more efficient packaging, while reducing weight and complexity of deployment mechanisms. These Collapsible Tubular Masts (CTMs), with a flight heritage since the Apollo missions [3], can be flattened along their length and coiled for a compact stowage configuration. The constraints applied to maintain this configuration are then removed, allowing the strain energy acquired during the applied packaging deformation to initiate deployment. As a result, very little actuation is required to achieve the final operational configuration, thereby reducing the number of deployment elements required and increasing reliability. Although deformable booms have historically been manufactured from thin metal sheets, carbon fiber reinforced plastic (CFRP) materials have been of interest to improve deployable boom performance for the last few decades.

CFRP booms fabricated from high strain thin-ply laminates are currently under investigation by

NASA for CubeSat applications, namely solar sailing [4]. When compared to their metallic counterparts, high strain thin-ply composite furlable booms are capable of enduring much larger curvatures and can be rolled to a smaller diameter for compact stowage [5]. In addition, lay-ups comprised of spread tow fabric, with ply thickness as small as 0.02 mm [6], are less likely to acquire any damage or delamination during this packaging process. CFRP materials also posses a near zero coefficient of thermal expansion, a property which must be especially considered for metallic deployables in drastically fluctuating thermal environments such as low earth orbit [7]. Lastly, the large specific stiffness of composites allows for overall weight to be reduced while maintaining deployed stiffness. With the low-cost of development and additional design freedom to create optimal lay-up configurations, CFRP booms are an attractive option to increase CubeSat potential, while maintaining the strict size and mass constraints enforced by secondary payload adapters.

The effects of long-term stowage are a present matter of interest for deformable deployable booms, as they can be subjected to stowage periods on the order of months or even years. The current investigations into the stowage problem for composite booms could be traced to the initial failed deployment of the lenticular jointed MARSIS antenna on the Mars Express, where it was discovered that significant stress relaxation during the two years it was packaged resulted in a complete stall of boom deployment [8]. This event illustrated the need for careful consideration of creep and stress relaxation effects during long-term stowage, particularly for booms which make use of packaging strain for much of the deployment energy. Although these effects may not end in the severe case observed by the Mars Express, accuracy of final deployed shape may be compromised, which in turn can cause dramatic reductions in deployed stiffness if the cross section is not sufficiently recovered.

The focus of this work is to implement and validate a numerical model so that it may be utilized in the analysis of thin-ply composite deployable structures. For comparison, a similar approach previously taken towards acquiring an exact solution for relaxation and creep recovery of a viscoelastic structure is utilized for a thin-ply composite plate under pure bending. Furthermore, the Column Bending Test is also modeled such that relaxation tests of thin-ply composite coupons can be compared against the numerical model.

CHAPTER 2: LITERATURE REVIEW

The mechanics and dynamics of a more simple form of self-deployable structural element, known as tape springs, has been well researched and documented [9] [10]. These shell structures, which are straight and transversely curved in their unloaded configuration as shown in 2.1, exhibit a reversible buckling behavior when folded. Tape springs can return to their initial geometry by simply releasing the folding constraints, utilizing the strain energy acquired during folding for deployment.

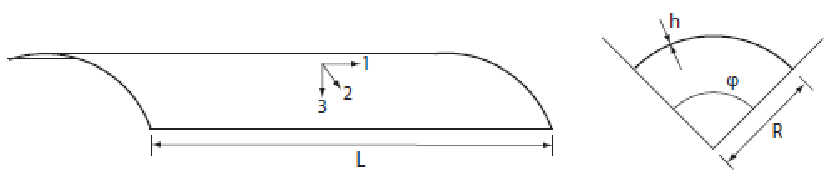

Figure 2.1: Tape spring geometry

As CFRP laminates became of interest for self-deployable structures, an emphasis was placed on investigating the effects of stress relaxation on deployment characteristics. Stress relaxation in CFRPs are inherited from the viscoelastic properties of the polymer matrix, therefore initial efforts were spent investigating the effect of a polymer's viscoelastic properties on an isotropic tape spring by Kwok et. al [11]. As a result of this work, deployment behavior of a tape spring after being folded for varying time at different temperatures was able to be reasonably predicted by utilizing the polymers viscoelastic properties in a finite element model.

Although deployment dynamics are an important characteristic of the structure, shape recovery after deployment determines the operational stiffness. Since post-deployment boundary conditions are that of an unloaded structure, this phase consists of creep recovery behavior under zero forces and moments. Creep compliance of the material is not sufficient to determine this behavior, however, as Kwok has previously shown that the shape recovery of an isotropic viscoelastic beam also depends on the relaxation modulus, applied deformation, and the total time and temperature during deformation [12]. The analytical solution provided by this work gives insight into the shape recovery of a viscoelastic structure, however, it's application is limited to only isotropic materials under small deformations (ie, one-dimensional linear viscoelasticity). Since large deformation numerical analysis of composite deployables is required, however, a more generalized material model is desired.

CHAPTER 3: METHODOLOGY

Theoretical background

In order to understand the behavior of thin structural elements fabricated from anisotropic viscoelastic materials, the constitutive equations of linear viscoelasticity is first reviewed. For materials exhibiting linear viscoelastic behavior, stress at any time t can be calculated by the Boltzman superposition integral:

$$\sigma_i(t) = \int_0^t C_{ij}(t-\tau)\frac{d\varepsilon_j}{d\tau}d\tau, \tag{3.1}$$

where σ and ε are the stress and strain tensors in Voigt notation, C_{ij} is the 6x6 relaxation modulus tensor, and τ is the variable of integration. Each entry in C_{ij} are functions of time and temperature, and as in elasticity theory, the number of independent entries depends on material symmetry. The reciprocal stress-strain relationship can be expressed in terms of the creep compliance tensor, S_{ij}:

$$\varepsilon_i(t) = \int_0^t S_{ij}(t-\tau)\frac{d\sigma_j}{d\tau}d\tau, \tag{3.2}$$

Each entry of C_{ij} and S_{ij} are represented by a prony series, so that their values can be calculated at a particular time by:

$$C_{ij}(t) = C_{ij,\infty} + \sum_{k=1}^{K} C_{ij,k}\exp\left(\frac{-t}{a_t\rho_k}\right) \tag{3.3}$$

$$S_{ij}(t) = S_{ij,0} + \sum_{k=1}^{K} S_{ij,k}\left[1-\exp\left(\frac{-t}{a_t\lambda_k}\right)\right] \tag{3.4}$$

Where $C_{ij,\infty}$ are the long term moduli, $S_{ij,0}$ are the instantaneous creep compliances, $C_{ij,k}$ and $S_{ij,k}$ are the prony coefficients, K is the number of prony coefficients, and ρ_k and λ_k are the relaxation and retardation times, respectively. Temperature effects are accounted for by a time shift factor, a_t, which can be approximated by the Arrhenious law equation:

$$\log(\mathrm{a_t}) = -\frac{E_a}{2.303R}(\frac{1}{T} - \frac{1}{T_0}) \tag{3.5}$$

where log is of base ten, E_a is the activation energy, R is the universal gas constant, T is the current temperature, and T_0 is the reference temperature. Utilizing Eq. (3.5) has the benefit of allowing changes in temperature to be considered by a single additional parameter. Qualitatively, an increase in temperature results in an acceleration of creep and relaxation effects, which is analytically accounted for by a shift in time scale. If the same shift factor applies to all relaxation and retardation times, the material is termed thermorheologically simple, which is assumed to apply to composites herein. The validity of applying this assumption to thin composite laminates has been previously been shown [13].

We begin constructing the viscoelastic plate model by invoking kirchoff plate assumptions, which simplifies the strain field:

$$\bar{\varepsilon_1} = \bar{\varepsilon_1} + x_3\bar{\kappa_1} \qquad \varepsilon_2 = \bar{\varepsilon_2} + x_3\bar{\kappa_2} \qquad \varepsilon_6 = \varepsilon_{12} \tag{3.6}$$

$$\bar{\varepsilon_3} = \bar{\varepsilon_4} = \bar{\varepsilon_5} = 0 \tag{3.7}$$

where $\bar{\varepsilon}$ and $\bar{\kappa}$ are the strains and curvatures of the plate mid-surface, x_3 is the out-of-plane displacement from the mid-surface, and ε_{12} is the in-plane engineering shear strain. With this simplification, the force and moment resultants $\bar{N}$ and $\bar{M}$ can acquired by integrating stresses over the thickness of the plate, h, in the following manner:

$$\bar{N}_1 = \int_{-\frac{h}{2}}^{\frac{h}{2}} \sigma_1 dx_3 \qquad \bar{N}_2 = \int_{-\frac{h}{2}}^{\frac{h}{2}} \sigma_2 dx_3 \qquad \bar{N}_3 = \int_{-\frac{h}{2}}^{\frac{h}{2}} \sigma_6 dx_3 \tag{3.8}$$

$$\bar{M}_1 = \int_{-\frac{h}{2}}^{\frac{h}{2}} \sigma_1 x_3 dx_3 \qquad \bar{M}_2 = \int_{-\frac{h}{2}}^{\frac{h}{2}} \sigma_2 x_3 dx_3 \qquad \bar{M}_3 = \int_{-\frac{h}{2}}^{\frac{h}{2}} \sigma_6 x_3 dx_3 \tag{3.9}$$

The strain fields given by Eqs. (3.6) and (3.7) are substituted into Eq. (3.1). The resulting stress definitions are then plugged into the force and moment resultant defined by Eqs. (3.8) and (3.9) to acquire the viscoelastic plate model:

$$\bar{N}_\alpha(t) = \int_0^t A_{\alpha\beta}(t-\tau)\frac{d\bar{\varepsilon}_\beta}{d\tau}d\tau + \int_0^t B_{\alpha\beta}(t-\tau)\frac{d\bar{\kappa}_\beta}{d\tau}d\tau, \tag{3.10}$$

$$\bar{M}_\alpha(t) = \int_0^t B_{\alpha\beta}(t-\tau)\frac{d\bar{\varepsilon}_\beta}{d\tau}d\tau + \int_0^t D_{\alpha\beta}(t-\tau)\frac{d\bar{\kappa}_\beta}{d\tau}d\tau, \tag{3.11}$$

where the A, B, and D matrices are the extensional relaxation stiffness, extension-bending coupling relaxation stiffness, and bending relaxation stiffness, respectively, each with a size of 3-by-3. Here, α and β range from 1 to 3, with 1 and 2 representing in-plane directions, and 3 is the in-plane shear and twist for strain and curvatures, respectively. The reciprocal relationships to acquire strains and curvatures is defined as:

$$\bar{\varepsilon}_\alpha(t) = \int_0^t a_{\alpha\beta}(t-\tau)\frac{d\bar{N}_\beta}{d\tau}d\tau + \int_0^t b_{\alpha\beta}(t-\tau)\frac{d\bar{M}_\beta}{d\tau}d\tau, \tag{3.12}$$

$$\bar{\kappa}_\alpha(t) = \int_0^t c_{\alpha\beta}(t-\tau)\frac{d\bar{N}_\beta}{d\tau}d\tau + \int_0^t d_{\alpha\beta}(t-\tau)\frac{d\bar{M}_\beta}{d\tau}d\tau, \tag{3.13}$$

where a is the extensional creep compliance, b and c are the extension-bending coupling creep compliances, and d is the bending creep compliance.

Numerical implementation

Since the form of the viscoelastic plate model is computationally expensive for a numerical model with many elements, a more efficient method for employing Eqs. (3.10) and (3.11) in finite element models is desired. In order to ensure finite element implementation of the viscoelastic plate model remains practical, we must first convert it to a more numerically efficient form. In order to accomplish this, the approach taken by Zocher et al. [14] towards Eq (3.1) is applied to Eqs. (3.10) and (3.11) to acquire an incremental form, which is as follows

$$\bar{N}_\alpha(t_{n+1}) = \bar{N}_\alpha(t_n) + \Delta\bar{N}_\alpha(t_{n+1}) \qquad \bar{M}_\alpha(t_{n+1}) = \bar{M}_\alpha(t_n) + \Delta\bar{M}_\alpha(t_{n+1}) \tag{3.14}$$

where $\bar{N}_\alpha(t_{n+1})$ and $\bar{M}_\alpha(t_{n+1})$ are the force and moment resultants of an individual element at the current time increment and t_{n+1} and t_n is the time at the current and previous increments, respectively. The incremental change in force and moment resultants, $\Delta\bar{N}_\alpha(t_{n+1})$ and $\Delta\bar{M}_\alpha(t_{n+1})$, are calculated by:

$$\Delta\bar{N}_\alpha(t_n) = A'_{\alpha\beta}(t_{n+1})\Delta\varepsilon_\beta(t_{n+1}) + B'_{\alpha\beta}(t_{n+1})\Delta\kappa_\beta(t_{n+1}) - \Delta N^R_\alpha(t_n) \tag{3.15}$$

$$\Delta\bar{M}_\alpha(t_n) = B'_{\alpha\beta}(t_{n+1})\Delta\varepsilon_\beta(t_{n+1}) + D'_{\alpha\beta}(t_{n+1})\Delta\kappa_\beta(t_{n+1}) - \Delta M^R_\alpha(t_n) \tag{3.16}$$

Here, $\Delta\varepsilon_\beta$ and $\Delta\kappa_\beta$ are the changes in shell section strains and curvatures between the previous and current increment, which are assumed be linear over time. The remainder of the terms in Eqs. (3.15) and (3.16) are given by:

$$A'_{\alpha\beta} = A_{\alpha\beta,\infty} + \frac{1}{\Delta t_{n+1}} \sum_{k=1}^{K} \rho_k A_{\alpha\beta,k} [1 - \exp(\frac{-\Delta t_{n+1}}{\rho_k})] \tag{3.17}$$

$$B'_{\alpha\beta} = B_{\alpha\beta,\infty} + \frac{1}{\Delta t_{n+1}} \sum_{k=1}^{K} \rho_k B_{\alpha\beta,k} [1 - \exp(\frac{-\Delta t_{n+1}}{\rho_k})] \tag{3.18}$$

$$D'_{\alpha\beta} = D_{\alpha\beta,\infty} + \frac{1}{\Delta t_{n+1}} \sum_{k=1}^{K} \rho_k D_{\alpha\beta,k} [1 - \exp(\frac{-\Delta t_{n+1}}{\rho_k})] \tag{3.19}$$

$$\Delta N^R_{\alpha}(t_n) = \sum_{k=1}^{K} [1 - \exp(\frac{-\Delta t_n}{\rho_k})] \sum_{\beta=1}^{3} [T_{\alpha\beta,k}(t_n) + U_{\alpha\beta,k}(t_n)] \tag{3.20}$$

$$\Delta M^R_{\alpha}(t_n) = \sum_{k=1}^{K} [1 - \exp(\frac{-\Delta t_n}{\rho_k})] \sum_{\beta=1}^{3} [V_{\alpha\beta,k}(t_n) + W_{\alpha\beta,k}(t_n)] \tag{3.21}$$

where $T_{\alpha\beta}$, $U_{\alpha\beta}$, $V_{\alpha\beta}$, and $W_{\alpha\beta}$ are vectors of length K, which are stored to be used at the next time increment once they are calculated by:

$$T_{\alpha\beta,k}(t_n) = T_{\alpha\beta,k}(t_{n-1}) \exp(\frac{-\Delta t_n}{\rho_k}) + \rho_k A_{\alpha\beta,k} (\frac{\Delta \varepsilon_{\beta}(t_n)}{\Delta t_n}) [1 - \exp(\frac{-\Delta t_n}{\rho_k})] \tag{3.22}$$

$$U_{\alpha\beta,k}(t_n) = U_{\alpha\beta,k}(t_{n-1}) \exp(\frac{-\Delta t_n}{\rho_k}) + \rho_k B_{\alpha\beta,k} (\frac{\Delta \kappa_{\beta}(t_n)}{\Delta t_n}) [1 - \exp(\frac{-\Delta t_n}{\rho_k})] \tag{3.23}$$

$$V_{\alpha\beta,k}(t_n) = V_{\alpha\beta,k}(t_{n-1})\exp(\frac{-\Delta t_n}{\rho_k}) + \rho_k B_{\alpha\beta,k}(\frac{\Delta\varepsilon_\beta(t_n)}{\Delta t_n})[1-\exp(\frac{-\Delta t_n}{\rho_k})] \tag{3.24}$$

$$W_{\alpha\beta,k}(t_n) = W_{\alpha\beta,k}(t_{n-1})\exp(\frac{-\Delta t_n}{\rho_k}) + \rho_k D_{\alpha\beta,k}(\frac{\Delta\kappa_\beta(t_n)}{\Delta t_n})[1-\exp(\frac{-\Delta t_n}{\rho_k})] \tag{3.25}$$

To consider temperature effects in the numerical model, time-temperature superposition can be employed. The reduced time, t', is calculated by simply dividing the current time t by the shift factor a_t as described in Eq. (3.5). As a result, the reduced time step $\Delta t'$ can be calculated simply as:

$$\Delta t'_n = \frac{\Delta t_n}{a_t} \tag{3.26}$$

The jacobian, or tangent stiffness, of a finite element shell section, J, is a 6-by-6 matrix defined as the derivative of the section forces and moments of the current time step with respect to the current strains and curvatures, that is:

$$J_{\alpha\beta} = \frac{\partial F_\alpha(t_{n+1})}{\partial E_\beta(t_{n+1})} \tag{3.27}$$

where

$$F = \begin{bmatrix} \bar{N} \\ \bar{M} \end{bmatrix}, \tag{3.28}$$

and

$$E = \begin{bmatrix} \bar{\varepsilon} \\ \bar{\kappa} \end{bmatrix} \tag{3.29}$$

Applying Eq. (3.27) to Eqs. (3.15) and (3.16), only terms dependent on the current time step remain. By default, the jacobian matrix is symmetric in Abaqus [15], thus reducing the number of terms which must be computed. Non-symmetric tangent stiffness is not considered in this work.

The force/strain component of the stiffness matrix, which represents the upper left quadrant of the jacobian, is given by:

$$\frac{\partial N_\alpha(t_{n+1})}{\partial \varepsilon_\beta(t_{n+1})} = A_{\alpha\beta,\infty} + \frac{1}{\Delta t_{n+1}} \sum_{k=1}^{K} \rho_k A_{\alpha\beta,k}[1-\exp(\frac{-\Delta t_{n+1}}{\rho_k})] \tag{3.30}$$

Similarly, the bottom right portion of the jacobian, representing the moment/curvature portion of the tangent stiffness, is also given by:

$$\frac{\partial M_\alpha(t_{n+1})}{\partial \kappa_\beta(t_{n+1})} = D_{\alpha\beta,\infty} + \frac{1}{\Delta t_{n+1}} \sum_{k=1}^{K} \rho_k D_{nm,k}[1-\exp(\frac{-\Delta t_{n+1}}{\rho_k})] \tag{3.31}$$

The iterative procedure described for calculating section forces and moments in terms of section strains and curvatures was implemented in Abaqus 2017 via a user generalized shell section subroutine (UGENS). The subroutine was written in Fortran and is shown in Appendix A.

Analytical solution for a composite viscoelastic plate

In order to validate the numerical model, an exact solution is desired. A simple case of a flat composite plate under pure bending is examined for comparison. As illustrated by Eqs. (3.10) and (3.11), the current state of viscoelastic material not only depends on the current loading or deformation, but also their histories. Boundary conditions for strain energy deployable booms would traditionally consist of applied displacements/rotations to achieve the stowage configuration, then switching to a prescribed zero force/moment for deployment. To acquire the true creep recovery after deployment, the entire history of the aforementioned boundary conditions must be considered.

Beginning with a composite plate initially unloaded, the stowage configuration is assumed to be achieved as a step input. The effects on neglecting the time history during which deformation is applied has previously shown to be negligible after a period of ten times the loading history [12]. The time history of curvatures up to the end of stowage are therefore:

$$\bar{\kappa}_1 = \kappa_s H(0), \qquad \bar{\kappa}_2 = \bar{\kappa}_3 = 0, \qquad\qquad t < t_s \tag{3.32}$$

where κ_s is the curvature applied for stowage, t_s is the stowage time, and H is the heaviside step function. Plugging the time history into Eqs. (3.10) and (3.11), we acquire the force and moment relaxation during stowage:

$$\bar{N}_\alpha(t) = B_{\alpha 1}(t)\kappa_s \tag{3.33}$$

$$\bar{M_\alpha}(t) = D_{\alpha 1}(t)\kappa_s \tag{3.34}$$

As previously mentioned, force and moments must be defined as zero in order to achieve deployment. Again, we assume this occurs instantaneously to acquire the complete force and moment time histories:

$$\bar{N_\alpha}(t) = B_{\alpha 1}(t)\kappa_s[1 - H(t - t_s)] \tag{3.35}$$

$$\bar{M_\alpha}(t) = D_{\alpha 1}(t)\kappa_s[1 - H(t - t_s)] \tag{3.36}$$

Plugging Eqs. (3.35) and (3.36) into Eq. (3.13), we achieve the following representation for bending creep recovery:

$$\bar{\kappa_1}(t) = \kappa_s[1 - I_\kappa - II_\kappa], \qquad t > t_s \tag{3.37}$$

where

$$I_\kappa = d_{1\alpha}(t - t_s)D_{\alpha 1}(t_s) + \int_{t_s}^{t} d_{1\alpha}(t - \tau)\frac{dD_{\alpha 1}}{d\tau}d\tau \tag{3.38}$$

$$II_\kappa = c_{1\alpha}(t - t_s)B_{\alpha 1}(t_s) + \int_{t_s}^{t} c_{1\alpha}(t - \tau)\frac{dB_{\alpha 1}}{d\tau}d\tau \tag{3.39}$$

For a comparison between the exact solutions for moment relaxation during stowage and creep recovery in Eqs. (3.34) and (3.37) with the numerical approximation described in section 3, a finite element analysis is conducted for a square composite plate under pure bending. The *ABD* relaxation matrix for a four-ply plain weave thin-ply CFRP fabricated from M30S fabric pre-impregnated with Patz Materials and Technology's F7 resin is utilized, which has been previously determined [16]. Since this composite laminate is balanced and symmetric about the plate mid-surface, the *B*, *b* and *c* coupling matrices are zero and thus the exact solution is simplified. The *A* and *D* relaxation matrices were used in the UGENS subroutine previously described. The prony coefficients used are shown in Table 3.1.

Table 3.1: Long term moduli and prony coefficients for a $[0/90]_4$ plain weave thin-ply composite in Newtons, millimeters, and seconds

i	$\rho_i(seconds)$	A_{11i} (N/mm)	A_{12i} (N/mm)	A_{33i} (N/mm)	D_{11i} (N)	D_{12i} (N)	D_{33i} (N)
∞	-	15418.47	614.19	48.70	77.63	0.20	0.22
1	1.89E+01	37.19	9.43	14.41	0.13	0.05	0.06
2	1.00E+02	95.54	23.39	36.28	0.34	0.12	0.16
3	1.00E+03	139.44	30.92	50.08	0.48	0.16	0.22
4	2.00E+04	62.61	13.55	22.27	0.22	0.07	0.10
5	1.00E+05	98.06	19.31	33.01	0.33	0.11	0.15
6	1.95E+06	59.46	11.45	20.06	0.20	0.06	0.09
7	1.77E+07	47.94	8.63	14.94	0.15	0.05	0.07
8	1.74E+08	193.82	36.91	65.91	0.65	0.21	0.29
9	1.38E+09	280.85	33.67	72.31	0.79	0.24	0.32
10	1.00E+10	243.42	29.63	76.87	0.80	0.25	0.34
11	1.00E+11	571.16	4.30	85.60	1.13	0.28	0.38
12	1.00E+12	166.29	1.81E-09	84.63	0.85	0.27	0.38
13	1.00E+13	1943.60	4.44E-08	113.95	2.46	0.37	0.51
14	1.00E+14	683.26	1.54E-07	6.33	0.69	0.01	0.03

A 100 mm x 100 mm plate was defined in Abaqus and meshed with 400 S4R elements with a maximum dimension of 5 mm. To generate the entire history, the analysis was conducted in four static steps: Bending, Stowage, Deployment, and Recovery. During the bending step, opposite rotations of 45 degrees were applied to the top and bottom edges of the plate shown in Fig. 3.1 over a period of 10 seconds, and this configuration was maintained for two years for the stowage step. For deployment, the bottom edge boundary condition was maintained, and reaction forces and moments at the end of stowage were linearly ramped to zero over a period of 10 seconds. At the end of the deployment step, the plate was allowed an additional one year to recover. Reaction moments and end rotations were extracted during the stowage and recovery steps, respectively, to compare with solutions acquired from Eqs. (3.34) and (3.37).

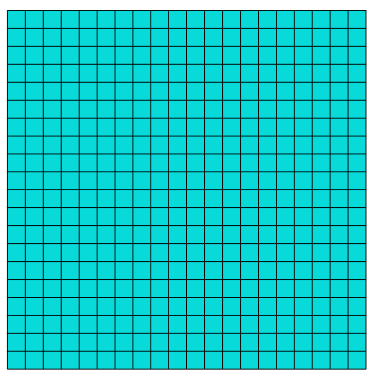

Figure 3.1: Finite element model of a composite plate

Column Bending Test

Up until recently, experimental testing of thin materials under bending have been challenging endeavor. With the development of the Column Bending Test (CBT) fixtures, however, the response of a thin-ply composite laminate under pure bending can be characterized by a simple experiment utilizing any common uniaxial testing machine [17]. CBT equations can be used to calculate moment and curvature as a function of crosshead displacement (δ), measured force (P), gauge length (s), coupon thickness (t), fixture rotation (ϕ), and dimensions of the CBT fixtures. The geometry of the CBT experiment is shown in 3.2.

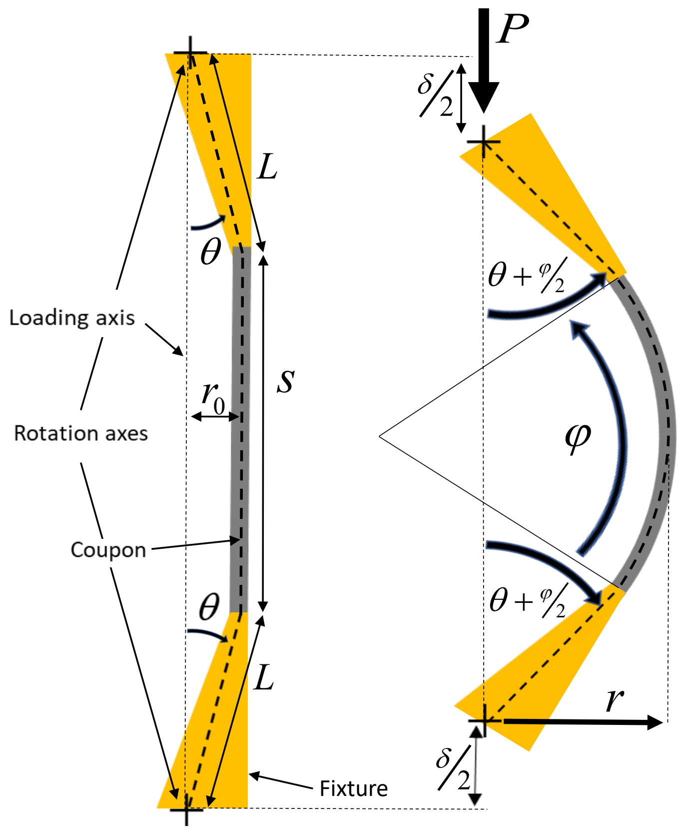

Figure 3.2: Column Bending Test geometry

The relationship between crosshead displacement and fixture rotations is given by:

$$\delta = s[1 - \frac{2}{\phi}\sin(\frac{\phi}{2})] + 2\mathrm{L}[\cos(\theta) - \cos(\theta + \frac{\phi}{2})] \tag{3.40}$$

Where L is the distance from pin axis to coupon clamped edge, and θ is the angle between the loading axis and a straight line from fixture pin to the mid-plane of the coupon clamped edge. The angle θ depends only on L and the coupon/pin axis offset at the beginning of the test r_0,

$$\tan(\theta) = \frac{r_0}{L} \tag{3.41}$$

Using the thickness of the coupon, t, the initial offset between loading axis and coupon mid-plane, r_0:

$$r_0 = 1.97866 + \frac{t}{2} \tag{3.42}$$

where r_0 and t are in millimeters, and 1.97866 represents the perpendicular distance between loading axis and nearest clamping surface. Once ϕ is determined, the curvature, κ at a particular configuration can be calculated by:

$$\kappa = \frac{\phi}{s} \tag{3.43}$$

To calculate the moment corresponding to the current curvature, the moment arm r must first be calculated as:

$$r = \frac{s}{\phi}[1 - \cos(\frac{\phi}{2})] + \mathrm{L}\sin(\theta + \frac{\phi}{2}) \tag{3.44}$$

The moment can then be calculated by

$$M = Pr \tag{3.45}$$

A Column Bending Test experiment was performed on a 0.267 mm thick 4-ply plain weave thin-ply coupon with a procedure similar to the previous flat plate bending simulations. Using a 25.51 mm wide coupon with a gauge length (s) of 32.15 mm. The fixtures were initially aligned and pinned in a Mechanical Testing System (MTS) uniaxial testing machine (Model C43-504), as shown in Fig. 3.3, which was used to monotonically drive the top fixture downwards while the bottom fixture remains fixed. Crosshead displacement and force measurements using a 25 N load cell were acquired at rate of 2 Hz. Temperature was controlled throughout the test by containing the coupon and fixtures assembly inside a Thermcraft environmental chamber (Model LBO-24-10-10-1T-J14642/1A) with Inconel covered air heaters controlled by a Eurotherm temperature controller (2404/CP/VH/LH/TC).

Figure 3.3: Column Bending Test setup

Experiments were carried out in five steps: thermal soak, load, relaxation, unloading, and creep recovery. During the thermal soak step, the chamber was heated to a temperature of 60° C and maintained for a period of one hour. During this period, load control was executed to adjust the crosshead and maintain a zero measured force, thus keeping the coupon unloaded. After the soak period, the crosshead was then driven downwards to achieve a curvature of 0.05 mm^{-1} over a period of 100 seconds. This configuration was then maintained for a period of one hour to observe the relaxation of the coupon. At the end of the relaxation period, the load was then reduced at a rate of 0.05 N/s until a zero force was measured by the load cell. This unloaded configuration was then maintained for two hours by again adjusting crosshead to keep a zero measured force during the creep recovery portion of the experiment.

The Column Bending Test geometry shown in Fig. 3.4 was modeled in Abaqus for a coupon with gauge length (s) of 34 mm and width of 25.4 mm. The coupon was meshed with S4R elements with a maximum dimension of 0.5 mm. To replicate the loading conditions, two reference points were defined which coincide with the intersection of testing machine loading axis and rotation axes of the CBT fixtures, which are offset from the plane of coupon in the initial configuration. The reference points were placed on the mid-line of the coupons gauge length with a perpendicular offset 25.4 mm from the free edge and 1.98 mm from the plane of the coupon. A rigid body tie was defined between the coupon free edges and their respective reference nodes to simulate the geometry of the CBT fixtures.b

The *ABD* relaxation matrix of the 4-ply plain weave composite was also used in the Column Bending Test simulation. To account for temperature changes in the material, Eq. (3.5) was utilized in the subroutine, using the experimentally determined activation energy of the epoxy matrix ($E_a = 170kJ/mol$).

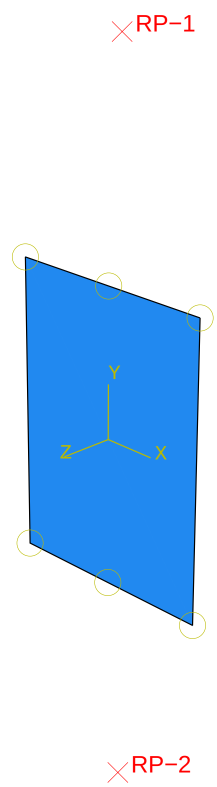

Figure 3.4: Column Bending Test model

The CBT simulation was carried out with a near identical procedure as the experiments, however, the thermal soak step was not simulated and instead the coupon was defined to be 60° C at the beginning of analysis via a predefined field. For the entirety of the simulation, reference point 2 (shown in Fig. 3.4) was given a pinned condition by prescribing all translations and rotations to be zero except for rotations about the x-axis, which was left free. The x-direction rotations of reference point 1 was also left free for the entire simulation, and only y-displacements were prescribed to simulate crosshead displacement. In the initial loading step shown in Fig. 3.5, a displacement of 24.345 mm was applied to reference point 1 over 120 seconds. The configuration at the end of the loading step was then maintained for one hour for the relaxation step. To unload the coupon, the reaction force at the end of the relaxation step were ramped to zero over 120 seconds.

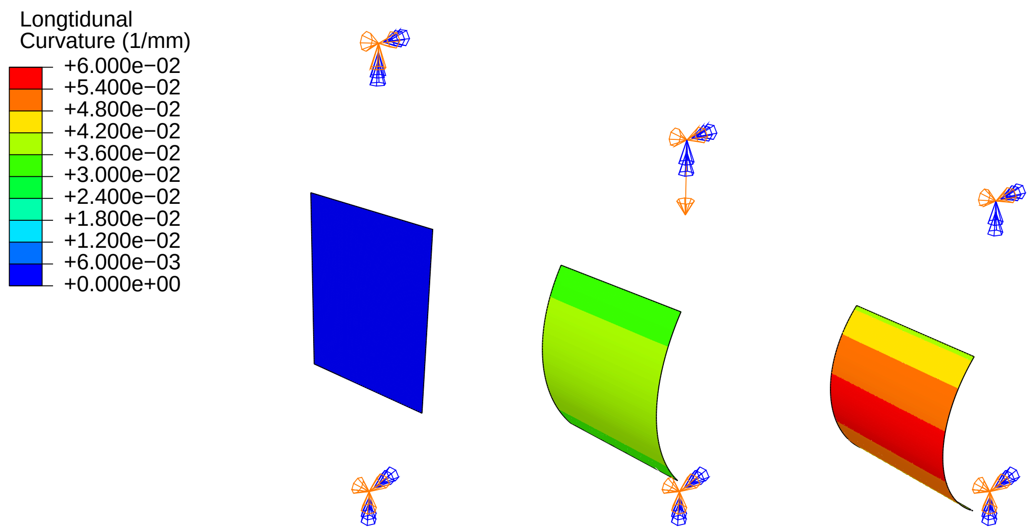

(a) (b) (c)

Figure 3.5: Longitudinal curvature during loading of Column Bending Test model in (a) initial configuration (b) halfway through loading (c) final configuration

CHAPTER 4: RESULTS

Moment relaxation results are compared in Fig. 4.1 for the exact solution and finite element simulation of the 4-ply flat composite plate under pure bending. During the two year relaxation period, almost no difference is observed between the two solutions. Similarly, in the one year period after the plates are unloaded, the solutions for residual curvature in the initial unloaded condition and their subsequent creep recovery are near identical, as shown in Fig. 4.2.

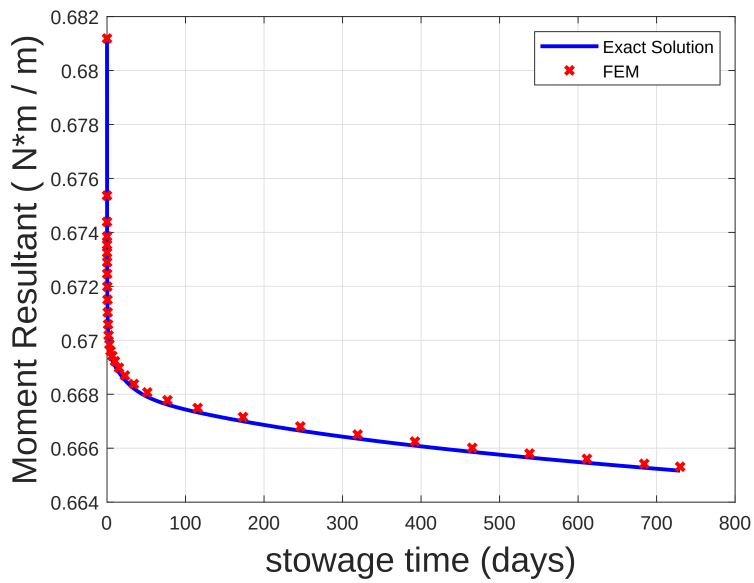

Figure 4.1: Moment relaxation for exact solution and FE model

Column Bending Test equations are used to compare moment and curvature between experimental and numerical results. Moment vs. curvature for both results are shown during the loading portion in Fig. 4.3. A slightly higher bending stiffness is observed in the experiment, as illustrated by the slightly steeper moment versus curvature line. This difference is attributed sample to sample variance in laminate thickness, which is prevalent in composites. Coupon thickness was measured to be 0.267 mm, whereas assumed thickness in the micromechanical model used to determine *ABD* relaxation was 0.228 mm.

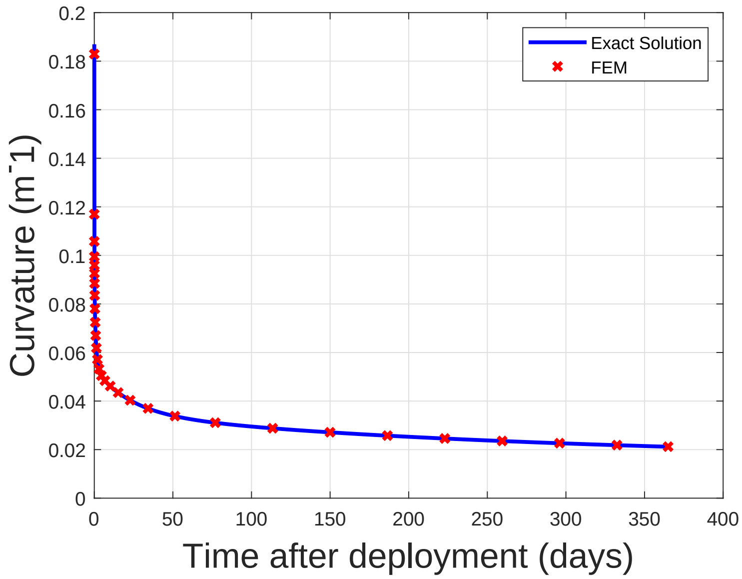

Figure 4.2: Creep recovery for exact solution and FE model

Contour plots of section moments at the beginning and end of the model relaxation portion is shown in Fig. 4.6. Due to the difference in bending stiffness during the loading period, moment relaxation becomes offset as shown in Fig. 4.7, however, the offset appears to be relatively constant. To better compare relaxation behavior, moment relaxation is normalized by the initial moment at the end of the loading step. Normalized moment relaxation is shown in Fig. 4.10, showing good agreement between the experiment and simulation.

Curvature and moment over time during the unloading portion for the experiment and simulation are shown in Figs. 4.5(a) and 4.5(b), respectively. Since force rate was used to control unloading in the experiment, and a slightly higher forces was measured at the end of the relaxation period, total time to unload in the experiment was slightly higher than that of the simulation. Also, as shown in Figs. 4.6(a) and 4.6(b), the difference in moment/curvature paths during unloading is attributed to the MTS software determining an initial crosshead rate to achieve the desired force

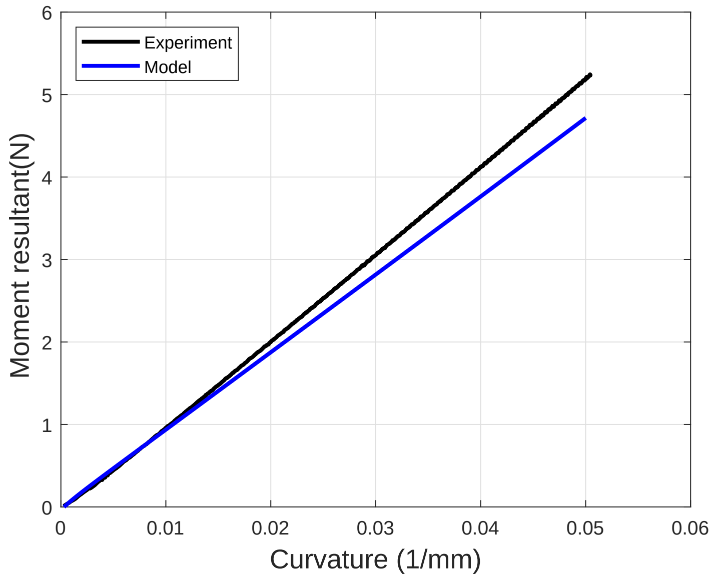

Figure 4.3: Moment vs. curvature during loading for experiment and simulation

rate. However, since the relationship between force and displacement is not linear, a constant force rate is not achieved in the entire unloading step. Fig. 4.6(b) illustrates the constant crosshead rate used to achieve the desired force rate shown measured over the first 60 seconds.

Curvature creep recovery behavior after the coupon is unloaded is compared between results obtained from the experiment and model is shown in Fig. 4.9. Despite the offset in moment relaxation, creep recovery of the unloaded coupon after the relaxation period shows good agreement between experimental values and those obtained from the numerical model. However, noise encountered after 1000 seconds of the recovery portion of the experiment represents a difference in crosshead position of approximately 0.045 mm, thereby adding some uncertainty in actual curvature due to very small relative crosshead positions. Curvature recovery is visualized by a longitudinal curvature contour plot during the first hour of the creep recovery portion of the Column Bending Test model, shown in Fig. 4.8.

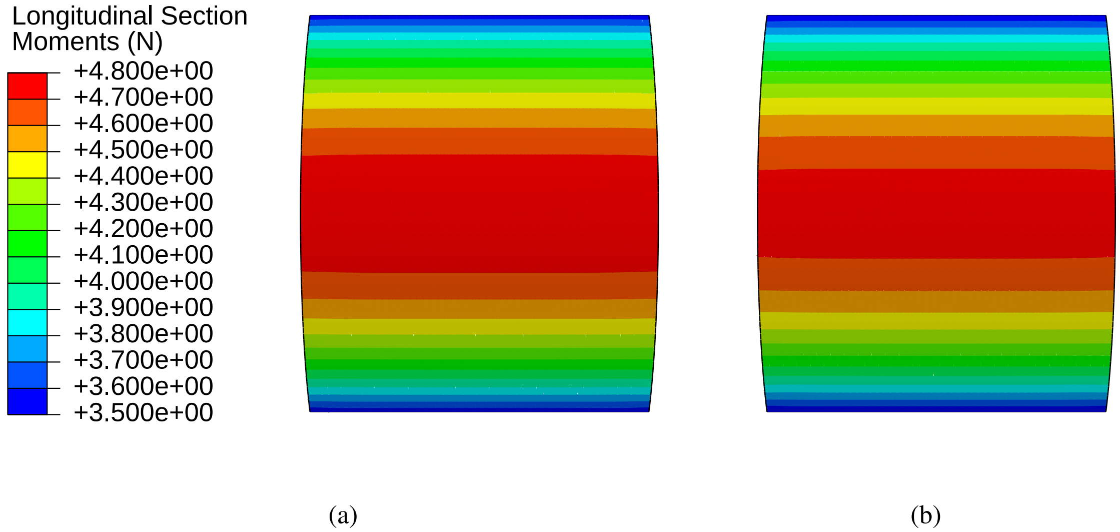

Figure 4.4: Longitudinal section moments at (a) the beginning and (b) end of relaxation period

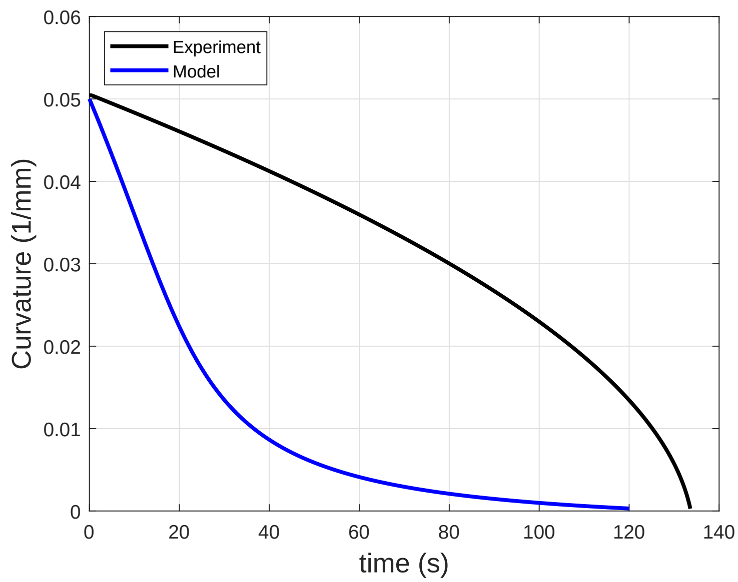

(a)

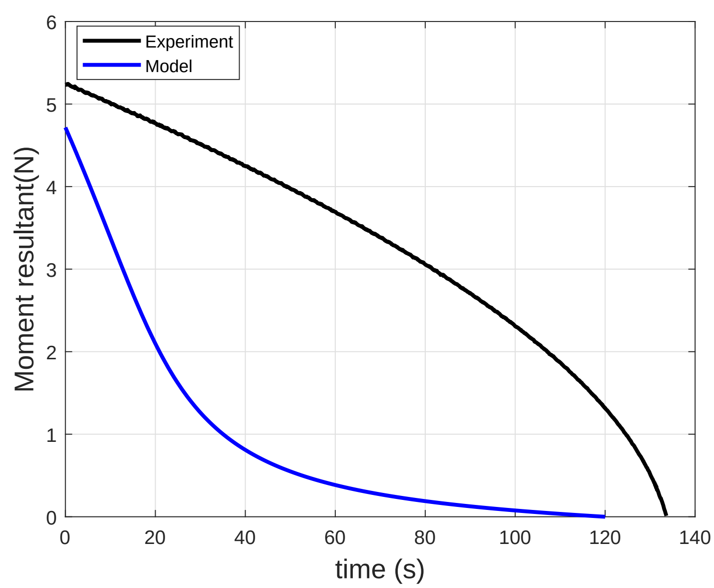

(b)

Figure 4.5: (a) Curvature and (b) moment vs. time during unloading

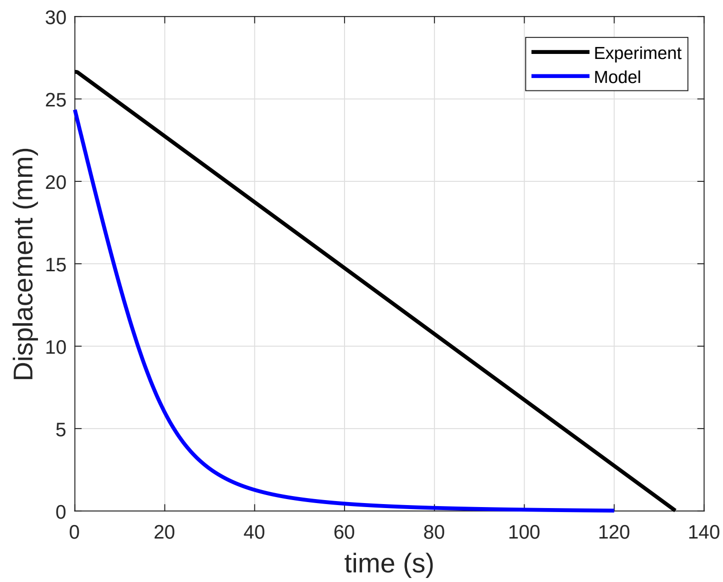

(a)

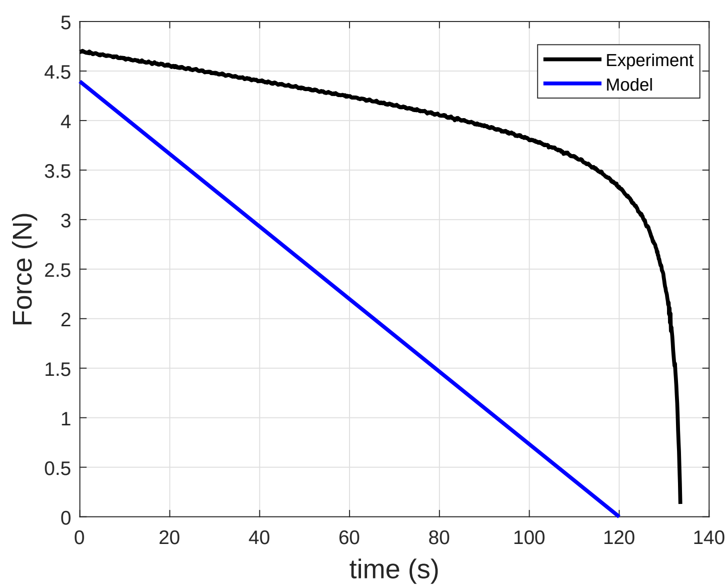

(b)

Figure 4.6: (a) Crosshead displacement and (b) reaction force vs. time during unloading

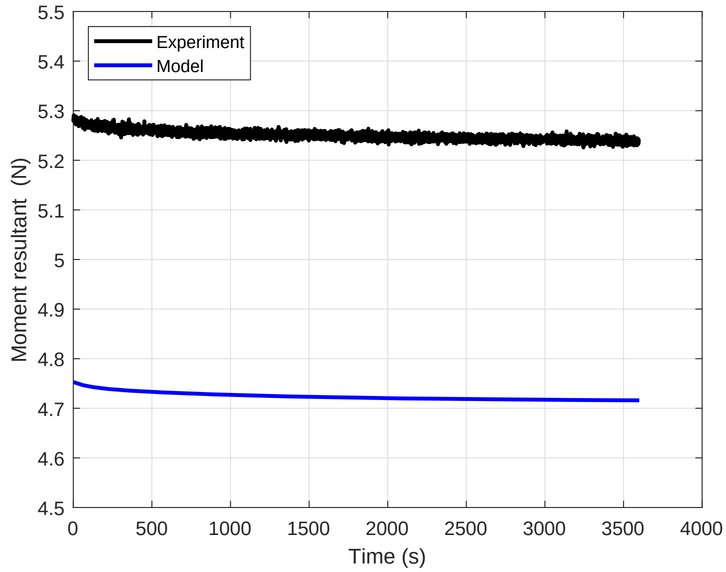

Figure 4.7: Moment relaxation for experiment and simulation

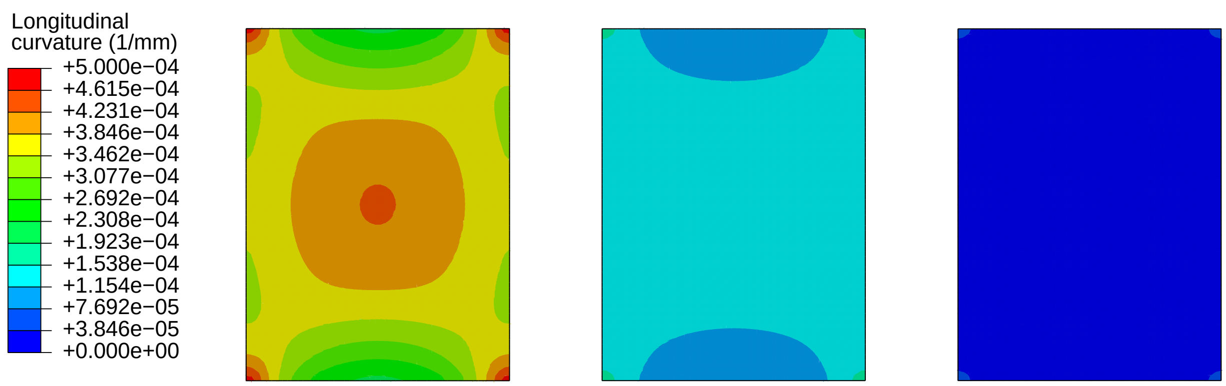

(a) (b) (c)

Figure 4.8: Longitudinal curvature during creep recovery in model (a) initially after being unloaded (b) after 15 minutes (c) after one hour

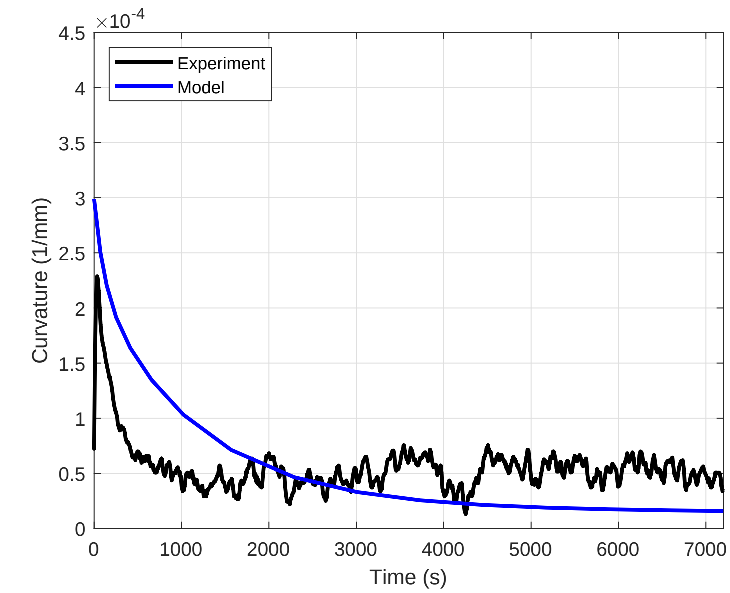

Figure 4.9: Creep recovery for experiment and simulation

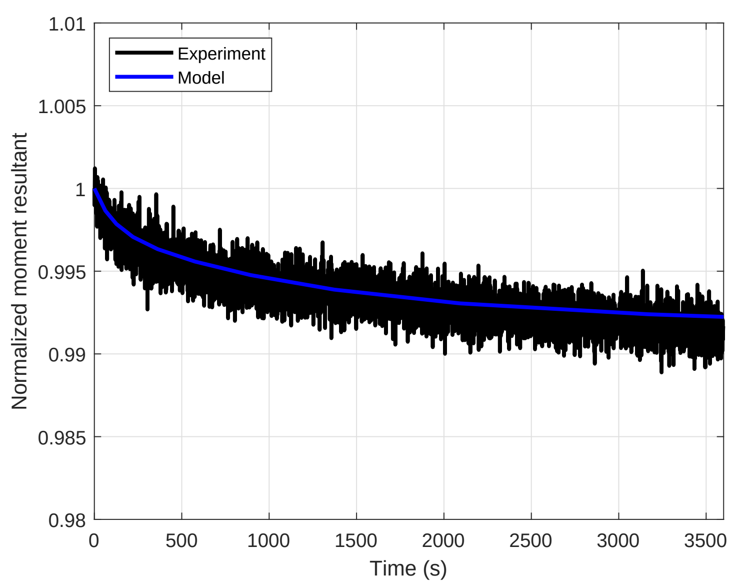

Figure 4.10: Normalized moment relaxation for experiment and simulation

CHAPTER 5: CONCLUSIONS

A numerical method for considering viscoelastic characteristics of thin-ply composites in finite element models was presented. The procedure utilizes an iterative process designed to reduce the computational cost of numerically calculating viscoelastic integrals. The numerical model was first applied to a square flat plate under pure bending for a relaxation and creep recovery analysis, using a previously determined *ABD* stiffness relaxation matrix of a 4-ply plain weave laminate. The results from the finite element analysis were compared against an exact solution which was also derived for a viscoelastic composite plate under the same boundary conditions. With near identical results acquired from the numerical model and exact solution, the validity and accuracy of the iterative method was confirmed.

To further validate the numerical model and the accuracy of applying time-temperature superposition to a thin-ply composite, a relaxation and creep recovery experiment at an elevated temperature of 60° C was conducted using Column Bending Test fixtures. A 4-ply plain weave thin-ply coupon was bent to a curvature of 0.05 mm^{-1} and kept in this configuration for a period of one hour, and subsequently unloaded such that a zero moment is applied. Once the coupon was unloaded, residual curvature and it's transient recovery was monitored over two hours with a zero load creep period. The Column Bending Test was modeled in Abaqus and compared with experimental data, using the curvature and moment values calculated from crosshead displacement and reaction force for a more direct comparison. A slightly larger bending stiffness was measured during the loading portion of the experiment than was observed in the finite element analysis. Due to the slightly higher moment measured at the end of loading, an offset was observed during the relaxation portion. Despite this offset, very similar curvature creep recovery was observed for both experimental and numerical results. The difference between numerical and experimental stiffness is attributed partly to a difference in coupon thickness versus the thickness assumed in the micromechanical model (0.267 mm vs. 0.228 mm, respectively).

In order to better capture the creep recovery behavior of a thin-ply composite coupon, photogrammatric measurements will be made to confirm the calculated curvature of the coupon during the recovery portion of future experiments. By measuring curvature directly using digital image correlation, uncertainty in curvature can be reduced significantly. To also better understand stiffness differences in experimental and numerical analysis, micrograph images will be taken of coupon cross sections after being tested, thereby allowing for fiber distribution in the material, voids, and other microscopic variances to be quantified and better explain numerical and experimental differences.

APPENDIX A: USER GENERALIZED SHELL SECTION SUBROUTINE

```
*USER SUBROUTINES
C*************************************************************************
C23456789012345678901234567890123456789012345678901234567890123456789012
      SUBROUTINE UGENS(DDNDDE,FORCE,STATEV,SSE,SPD,PNEWDT,STRAN,
     1 DSTRAN,TSS,TIME,DTIME,TEMP,DTEMP,PREDEF,DPRED,CENAME,NDI,
     2 NSHR,NSECV,NSTATV,PROPS,JPROPS,NPROPS,NJPROP,COORDS,CELENT,
     3 THICK,DFGRD,CURV,BASIS,NOEL,NPT,KSTEP,KINC,NIT,LINPER)

      INCLUDE 'ABA_PARAM.INC'

      CHARACTER*80 CMNAME
      DIMENSION DDNDDE(NSECV,NSECV),FORCE(NSECV),STATEV(NSTATV),
     1 STRAN(NSECV),DSTRAN(NSECV),TSS(2),TIME(2),PREDEF(*),
     2 DPRED(*),PROPS(*),JPROPS(*),COORDS(3),DFGRD(3,3),
     3 CURV(2,2),BASIS(3,3)

c      INTEGER nProny
      REAL*8 rhoi(14), n
      REAL*8 A11inf, A12inf, A13inf, A22inf, A23inf, A33inf
      REAL*8 D11inf, D12inf, D13inf, D22inf, D23inf, D33inf
      REAL*8 A11i(14), A12i(14), A13i(14), A22i(14), A23i(14), A33i(14)
      REAL*8 D11i(14), D12i(14), D13i(14), D22i(14), D23i(14), D33i(14)
      REAL*8 W11(14), W12(14), W13(14), W21(14), W22(14), W23(14)
      REAL*8 W31(14), W32(14), W33(14)
      REAL*8 U11(14), U12(14), U13(14), U21(14), U22(14), U23(14)
      REAL*8 U31(14), U32(14), U33(14)
      REAL*8 N1, N2, N3, M1, M2, M3
      REAL*8 NR1, NR2, NR3, MR1, MR2, MR3
      REAL*8 de1, de2, de3, dk1, dk2, dk3
      REAL*8 Ap11, Ap12, Ap13, Ap22, Ap23, Ap33
      REAL*8 Dp11, Dp12, Dp13, Dp22, Dp23, Dp33
      REAL*8 lamda(14), dt, a, Tref

C-----PROPS DESIGNATION----------C
C
C     PROPS  1 - 12  :  %A11inf, A12inf, A13inf... %Long term moduli
C     PROPS  13 - 19   : % relaxation times
C     PROPS  20 - 26 : A11i
C     PROPS  27 - 33 : A12i
C     PROPS  34 - 40 : A13i
C     PROPS  41 - 47 : A22i
C      PROPS  48 - 54 : A23i
C     PROPS  55 - 61 : A33i
C     PROPS  62 - 68 : D11i
C     PROPS  69 - 75 : D12i
C     PROPS  76 - 82 : D13i
C     PROPS  83 - 89 : D22i
C     PROPS  90 - 96 : D23i
C     PROPS  97 - 103 : D33i

C-----STATEV DESIGNATION----------C
C
C     STATEV  1 - 7    : W11i   % Moment Recursive terms (9 vectors of length nProny)
C     STATEV  8 - 14   : W12i
C     STATEV  15 - 21  : W13i
C     STATEV  22 - 28  : W21i
C     STATEV  29 - 35  : W22i
C     STATEV  36 - 42  : W23i
C     STATEV  43 - 49  : W31i
C     STATEV  50 - 56  : W32i
C     STATEV  57 - 63  : W33i
C     STATEV  64 - 70  : U11i   % Force recursive terms (9 vectors of length nProny)
C     STATEV  71 - 77  : U12i
C     STATEV  78 - 84  : U13i
```

```
C     STATEV  85 - 91  : U21i
C     STATEV  92 - 98  : U22i
C     STATEV  99 - 105  : U23i
C     STATEV  106 - 112  : U31i
C     STATEV  113 - 119  : U32i
C     STATEV  120 - 126  : U33i
C     STATEV  127 - 129  : NRi  Recursive Force
C     STATEV  130 - 132  : MRi  % Recursive Moments
C     STATEV  133 - 138 : N1, N2, N3, M1, M2, M3 %Forces and Moments from previous time step



C-----material parameters---------C

C      Number of Prony terms
      n = 14

C      Obtain long term modulus

       A11inf=PROPS(1)
       A12inf=PROPS(2)
      A13inf=PROPS(3)
      A22inf=PROPS(4)
      A23inf=PROPS(5)
      A33inf=PROPS(6)
       D11inf=PROPS(7)
       D12inf=PROPS(8)
      D13inf=PROPS(9)
      D22inf=PROPS(10)
      D23inf=PROPS(11)
      D33inf=PROPS(12)

C     Obtain Prony coefficients

      do i = 1,n
        rhoi(i)=PROPS(i+12)
        A11i(i)=PROPS(i + n*1 + 12)
        A12i(i)=PROPS(i + n*2 + 12)
        A13i(i)=PROPS(i + n*3 + 12)
        A22i(i)=PROPS(i + n*4 + 12)
        A23i(i)=PROPS(i + n*5 + 12)
        A33i(i)=PROPS(i + n*6 + 12)
        D11i(i)=PROPS(i+n*7+12)
        D12i(i)=PROPS(i+n*8+12)
        D13i(i)=PROPS(i+n*9+12)
        D22i(i)=PROPS(i+n*10+12)
        D23i(i)=PROPS(i+n*11+12)
        D33i(i)=PROPS(i+n*12+12)
      end do

C----------Inputs from previous time step (recursive terms and forces/moments)

C --------- Recursive Terms --------- C

      do i = 1,n
        W11(i)=STATEV(i)
        W12(i)=STATEV(i + n)
        W13(i)=STATEV(i + 2*n)
        W21(i)=STATEV(i + 3*n)
        W22(i)=STATEV(i + 4*n)
        W23(i)=STATEV(i + 5*n)
        W31(i)=STATEV(i + 6*n)
        W32(i)=STATEV(i + 7*n)
        W33(i)=STATEV(i + 8*n)
```

```
          U11(i)=STATEV(i + 9*n)
          U12(i)=STATEV(i + 10*n)
          U13(i)=STATEV(i + 11*n)
          U21(i)=STATEV(i + 12*n)
          U22(i)=STATEV(i + 13*n)
          U23(i)=STATEV(i + 14*n)
          U31(i)=STATEV(i + 15*n)
          U32(i)=STATEV(i + 16*n)
          U33(i)=STATEV(i + 17*n)
        end do

        NR1=STATEV(252)
        NR2=STATEV(253)
        NR3=STATEV(254)
        MR1=STATEV(255)
        MR2=STATEV(256)
        MR3=STATEV(257)
        N1=STATEV(258)
        N2=STATEV(259)
        N3=STATEV(260)
        M1=STATEV(261)
        M2=STATEV(262)
        M3=STATEV(263)

C       incremental generalized section strains/curvatures

        de1=DSTRAN(1)
        de2=DSTRAN(2)
        de3=DSTRAN(3)
        dk1=DSTRAN(4)
        dk2=DSTRAN(5)
        dk3=DSTRAN(6)

C --- Compute time increment dependent terms --- C
        Tref=30

        a=exp((170/(2.303*8.314462))*((1/TEMP)-(1/Tref)))

        dt=DTIME*a

        Ap11=A11inf
        Ap12=A12inf
        Ap13=A13inf
        Ap22=A22inf
        Ap23=A23inf
        Ap33=A33inf

        Dp11=D11inf
        Dp12=D12inf
        Dp13=D13inf
        Dp22=D22inf
        Dp23=D23inf
        Dp33=D33inf

        do i = 1,n
          lamda(i)=(1-exp(-dt/rhoi(i)))
          Ap11=Ap11+(1/dt)*(rhoi(i)*A11i(i))*lamda(i)
          Ap12=Ap12+(1/dt)*(rhoi(i)*A12i(i))*lamda(i)
          Ap13=Ap13+(1/dt)*(rhoi(i)*A13i(i))*lamda(i)
          Ap22=Ap22+(1/dt)*(rhoi(i)*A22i(i))*lamda(i)
          Ap23=Ap23+(1/dt)*(rhoi(i)*A23i(i))*lamda(i)
          Ap33=Ap33+(1/dt)*(rhoi(i)*A33i(i))*lamda(i)
          Dp11=Dp11+(1/dt)*(rhoi(i)*D11i(i))*lamda(i)
          Dp12=Dp12+(1/dt)*(rhoi(i)*D12i(i))*lamda(i)
```

```fortran
    Dp13=Dp13+(1/dt)*(rhoi(i)*D13i(i))*lamda(i)
    Dp22=Dp22+(1/dt)*(rhoi(i)*D22i(i))*lamda(i)
    Dp23=Dp23+(1/dt)*(rhoi(i)*D23i(i))*lamda(i)
    Dp33=Dp33+(1/dt)*(rhoi(i)*D33i(i))*lamda(i)
  end do




  do i = 1,n
    STATEV(i)=W11(i)*(exp(-dt/rhoi(i)))+
 & (rhoi(i)*D11i(i))*(dk1/dt)*lamda(i)
    STATEV(i+1*n)=W12(i)*(exp(-dt/rhoi(i)))+
 & (rhoi(i)*D12i(i))*(dk2/dt)*lamda(i)
    STATEV(i+2*n)=W13(i)*(exp(-dt/rhoi(i)))+
 & (rhoi(i)*D13i(i))*(dk3/dt)*lamda(i)
    STATEV(i+3*n)=W21(i)*(exp(-dt/rhoi(i)))+
 & (rhoi(i)*D12i(i))*(dk1/dt)*lamda(i)
    STATEV(i+4*n)=W22(i)*(exp(-dt/rhoi(i)))+
 & (rhoi(i)*D22i(i))*(dk2/dt)*lamda(i)
    STATEV(i+5*n)=W23(i)*(exp(-dt/rhoi(i)))+
 & (rhoi(i)*D23i(i))*(dk3/dt)*lamda(i)
    STATEV(i+6*n)=W31(i)*(exp(-dt/rhoi(i)))+
 & (rhoi(i)*D13i(i))*(dk1/dt)*lamda(i)
    STATEV(i+7*n)=W32(i)*(exp(-dt/rhoi(i)))+
 & (rhoi(i)*D23i(i))*(dk2/dt)*lamda(i)
    STATEV(i+8*n)=W33(i)*(exp(-dt/rhoi(i)))+
 & (rhoi(i)*D33i(i))*(dk3/dt)*lamda(i)
    STATEV(i+9*n)=U11(i)*(exp(-dt/rhoi(i)))+
 & (rhoi(i)*A11i(i))*(de1/dt)*lamda(i)
    STATEV(i+10*n)=U12(i)*(exp(-dt/rhoi(i)))+
 & (rhoi(i)*A12i(i))*(de2/dt)*lamda(i)
    STATEV(i+11*n)=U13(i)*(exp(-dt/rhoi(i)))+
 & (rhoi(i)*A13i(i))*(de3/dt)*lamda(i)
    STATEV(i+12*n)=U21(i)*(exp(-dt/rhoi(i)))+
 & (rhoi(i)*A12i(i))*(de1/dt)*lamda(i)
    STATEV(i+13*n)=U22(i)*(exp(-dt/rhoi(i)))+
 & (rhoi(i)*A22i(i))*(de2/dt)*lamda(i)
    STATEV(i+14*n)=U23(i)*(exp(-dt/rhoi(i)))+
 & (rhoi(i)*A23i(i))*(de3/dt)*lamda(i)
    STATEV(i+15*n)=U31(i)*(exp(-dt/rhoi(i)))+
 & (rhoi(i)*A13i(i))*(de1/dt)*lamda(i)
    STATEV(i+16*n)=U32(i)*(exp(-dt/rhoi(i)))+
 & (rhoi(i)*A23i(i))*(de2/dt)*lamda(i)
    STATEV(i+17*n)=U33(i)*(exp(-dt/rhoi(i)))+
 & (rhoi(i)*A33i(i))*(de3/dt)*lamda(i)
  end do

  NR1=0
  NR2=0
  NR3=0
  MR1=0
  MR2=0
  MR3=0


  do i = 1,n
    NR1=NR1+lamda(i)*(U11(i)+U12(i)+U13(i))
    NR2=NR2+lamda(i)*(U21(i)+U22(i)+U23(i))
    NR3=NR3+lamda(i)*(U31(i)+U32(i)+U33(i))
    MR1=MR1+lamda(i)*(W11(i)+W12(i)+W13(i))
```

```
          MR2=MR2+lamda(i)*(W21(i)+W22(i)+W23(i))
          MR3=MR3+lamda(i)*(W31(i)+W32(i)+W33(i))
        end do

        STATEV(252)=NR1
        STATEV(253)=NR2
        STATEV(254)=NR3
        STATEV(255)=MR1
        STATEV(256)=MR2
        STATEV(257)=MR3


C       Force and Moment Outputs

        N1=N1+Ap11*de1+Ap12*de2+Ap13*de3-NR1
        N2=N2+Ap12*de1+Ap22*de2+Ap23*de3-NR2
        N3=N3+Ap13*de1+Ap23*de2+Ap33*de3-NR3
        M1=M1+Dp11*dk1+Dp12*dk2+Dp13*dk3-MR1
        M2=M2+Dp12*dk1+Dp22*dk2+Dp23*dk3-MR2
        M3=M3+Dp13*dk1+Dp23*dk2+Dp33*dk3-MR3

        FORCE(1)=N1
        FORCE(2)=N2
        FORCE(3)=N3
        FORCE(4)=M1
        FORCE(5)=M2
        FORCE(6)=M3

        STATEV(258)=N1
        STATEV(259)=N2
        STATEV(260)=N3
        STATEV(261)=M1
        STATEV(262)=M2
        STATEV(263)=M3


C-----update Jacobian (tangent stiffess)-----C


        DDNDDE(1,1) = A11inf
        DDNDDE(1,2) = A12inf
        DDNDDE(1,3) = A13inf
        DDNDDE(2,2) = A22inf
        DDNDDE(3,3) = A33inf
        DDNDDE(4,4) = D11inf
        DDNDDE(4,5) = D12inf
        DDNDDE(4,6) = D13inf
        DDNDDE(5,5) = D22inf
        DDNDDE(6,6) = D33inf


        do i = 1, n
          DDNDDE(1,1)=DDNDDE(1,1)+A11i(i)*lamda(i)/(dt/rhoi(i))
          DDNDDE(1,2)=DDNDDE(1,2)+A12i(i)*lamda(i)/(dt/rhoi(i))
          DDNDDE(1,3)=DDNDDE(1,3)+A13i(i)*lamda(i)/(dt/rhoi(i))
          DDNDDE(2,2)=DDNDDE(2,2)+A22i(i)*lamda(i)/(dt/rhoi(i))
          DDNDDE(3,3)=DDNDDE(3,3)+A33i(i)*lamda(i)/(dt/rhoi(i))
          DDNDDE(4,4)=DDNDDE(4,4)+D11i(i)*lamda(i)/(dt/rhoi(i))
          DDNDDE(4,5)=DDNDDE(4,5)+D12i(i)*lamda(i)/(dt/rhoi(i))
          DDNDDE(4,6)=DDNDDE(4,6)+D13i(i)*lamda(i)/(dt/rhoi(i))
          DDNDDE(5,5)=DDNDDE(5,5)+D22i(i)*lamda(i)/(dt/rhoi(i))
          DDNDDE(6,6)=DDNDDE(6,6)+D33i(i)*lamda(i)/(dt/rhoi(i))
        end do
```

```
      DDNDDE(2,1)=DDNDDE(1,2)
      DDNDDE(2,3)=DDNDDE(1,3)
      DDNDDE(3,1)=DDNDDE(1,3)
      DDNDDE(3,2)=DDNDDE(2,3)
      DDNDDE(5,4)=DDNDDE(4,5)
      DDNDDE(5,6)=DDNDDE(4,6)
      DDNDDE(6,4)=DDNDDE(4,6)
      DDNDDE(6,5)=DDNDDE(5,6)




C      print *, DSTRAN(3)
C----------update energy----------C

C     update elastic strain energy in SSE
      SSE = 0.0

C     update plastic dissipation in SPD
       SPD = 0.0

      RETURN
      END
C**********************************************************************
C**********************************************************************
C23456789012345678901234567890123456789012345678901234567890123456789012
```

LIST OF REFERENCES

[1] A Hanaor and R Levy. Evaluation of deployable structures for space enclosures. *International Journal of Space Structures*, 16(4):211–229, 2001.

[2] BB Rennie. New closed tubular extendible boom. 1967.

[3] Rajnish Kumar and Shabeer Ahmed. Bending and flexing of the apollo 15 mass spectrometer boom. *Journal of Spacecraft and Rockets*, 9(12):940–942, 1972.

[4] Juan M Fernandez, Geoffrey K Rose, Casey J Younger, Gregory D Dean, Jerry E Warren, Olive R Stohlman, and W Keats Wilkie. Nasa's advanced solar sail propulsion system for low-cost deep space exploration and science missions that use high performance rollable composite booms. In *4th International Symposium on Solar Sailing*, Kyoto, Japan, 2017.

[5] Juan M Fernandez. Advanced deployable shell-based composite booms for small satellite structural applications including solar sails. In *4th International Symposium on Solar Sailing*, Kyoto, Japan, 2017.

[6] R Amacher, J Cugnoni, and J Botsis. Thin ply composites: experimental characterization and modeling. In *Proceedings of the 19th International Conference on Composite Materials (ICCM-19), Montreal*, pages 1–13, 2013.

[7] Olive R Stohlman and Erik R Loper. Thermal deformation of very slender triangular rollable and collapsible booms. 2016.

[8] M. Mobrem and D. Adams. Lenticular jointed antenna deployment anomaly and resolution onboard the mars express spacecraft. *Journal of Spacecraft and Rockets*, 46(2):403–410, 2009.

[9] KA Seffen, Z You, and S Pellegrino. Folding and deployment of curved tape springs. *International Journal of Mechanical Sciences*, 42(10):2055–2073, 2000.

[10] KA Seffen and S Pellegrino. Deployment dynamics of tape springs. *Proceedings of the Royal Society of London. Series A: Mathematical, Physical and Engineering Sciences*, 455(1983):1003–1048, 1999.

[11] K. Kwok and S. Pellegrino. Folding, stowage, and deployment of viscoelastic tape springs. *AIAA journal*, 51(8):1908–1918, 2013.

[12] Kawai Kwok. Shape recovery of viscoelastic beams after stowage. *Mechanics Based Design of Structures and Machines*, 43(1):95–111, 2015.

[13] A. Gomez-Delrio and K. Kwok. Viscoelastic behavior of thin-ply composites for deployable structures. In *69th International Astronautical Congress*, page 2, Bremen, Germany, 2018. IAF.

[14] M. A. Zocher, S. E. Groves, and D. H. Allen. A three-dimensional finite element formulation for thermoviscoelastic orthotropic media. *International Journal For Numerical Methods in Engineering*, 40:2267–2288, 1997.

[15] DS Simulia. Abaqus 2017 documentation, 2017.

[16] M. Hamillage and K. Kwok. High curvature bending of viscoelastic thin-ply composites. In *Proceedings of the American Society for Composites—Thirty-fourth Technical Conference*, 2019.

[17] Juan M Fernandez and Thomas W Murphey. A simple test method for large deformation bending of thin high strain composite flexures. In *2018 AIAA Spacecraft Structures Conference*, page 0942, 2018.